ARTICLE IN PRESS

Nature Communications

https://doi.org/10.1038/s41467-026-69609-4

Article in Press

A universal strategy towards self-healing materials via dynamic interfacial liquid metal coordination

Received: 2 September 2025

Accepted: 5 February 2026

Zhiwei Li, Yue Zhang, Songlin Liu, Jingyu Lan, Yan Peng & Jiuyang Zhang

Cite this article as: Li, Z., Zhang, Y., Liu, S. *et al.* A universal strategy towards self-healing materials via dynamic interfacial liquid metal coordination. *Nat Commun* (2026). https://doi.org/10.1038/s41467-026-69609-4

We are providing an unedited version of this manuscript to give early access to its findings. Before final publication, the manuscript will undergo further editing. Please note there may be errors present which affect the content, and all legal disclaimers apply.

If this paper is publishing under a Transparent Peer Review model then Peer Review reports will publish with the final article.

ARTICLE IN PRESS

© The Author(s) 2026. **Open Access** This article is licensed under a Creative Commons Attribution-NonCommercial-NoDerivatives 4.0 International License, which permits any non-commercial use, sharing, distribution and reproduction in any medium or format, as long as you give appropriate credit to the original author(s) and the source, provide a link to the Creative Commons licence, and indicate if you modified the licensed material. You do not have permission under this licence to share adapted material derived from this article or parts of it. The images or other third party material in this article are included in the article's Creative Commons licence, unless indicated otherwise in a credit line to the material. If material is not included in the article's Creative Commons licence and your intended use is not permitted by statutory regulation or exceeds the permitted use, you will need to obtain permission directly from the copyright holder. To view a copy of this licence, visit http://creativecommons.org/licenses/by-nc-nd/4.0/.

A Universal Strategy towards Self-Healing Materials *via* Dynamic Interfacial Liquid Metal Coordination

Zhiwei Li, [1,2] Yue Zhang, [1,2] Songlin Liu, [1,2] Jingyu Lan, [1,2] Yan Peng, [1,2,3] Jiuyang Zhang [1,2]*

[1] School of Chemistry and Chemical Engineering, Southeast University, Nanjing 211189, PR China

[2] National Graduate College for Elite Engineers, Southeast University, Wuxi Campus, Wuxi 214061, PR China

[3] Department of Mechanical Engineering & Materials Science, School of Engineering & Applied Science, Yale University; New Haven, CT. 06511, U.S.A.

* Corresponding authors

E-mail: jiuyang@seu.edu.cn

Abstract: Self-healing polymer materials, capable of autonomously repairing physical damage, have been broadly applied in modern technologies. In various self-healing systems, metal–ligand coordination bonds have been extensively utilized for their advantages of rich metal–ligand species and functionalities. However, common metal-ligand coordination either has excessively stable bond strengths or is too weak to construct self-healing materials. This work introduces coordination metals into liquid metals (LMs) to form multi-component LMs (mLMs), which creatively leverage the inherent fluidity of mLMs to convert common metal-ligand coordination (e.g., silver-sulfur and zinc/copper-imidazole systems) into reversible interfacial coordination. Such dynamic coordination successfully offers the fantastic self-healing efficiency over 90% for general polymers. Considering the ultra-high thermal conductivity of mLMs, self-healable thermal interface materials (TIMs) are obtained, which successfully address the long-standing challenge

of the irreversible damage in long-term used TIMs. The self-healable TIMs can lower the peak temperature of the central processing unit (CPU) by 20 ^oC under extreme conditions for long time (accumulated 16 hours thermal shock, -10 ^oC to 100 ^oC). This work provides a universal strategy for self-healing materials and greatly broadens the investigations of self-healing, coordination chemistry, liquid metal science, soft electronics, and thermal management materials.

Introduction

Self-healing polymer materials, owing to their inherent capacity for autonomous damage remediation, have emerged as indispensable constituents of modern intelligent material systems, such as wearable technologies, energy materials, and intelligent medical devices[1,2.] The current dominant strategy for achieving polymer self-healing properties involves introducing reversible covalent bonds (e.g., Diels-Alder reactions[3], disulfide bonds[4,5]), non-covalent bonds (e.g., hydrogen bonds[6-8], ionic bonds[9], host-guest interactions[10,11], coordination bonds[12-14]) and physical interactions (e.g., phase separation[15], magnetic force[16], shape memory effect[17]). These reversible interactions enable the fabrication of materials with high healing efficiency, spontaneous healing without external conditions, and functional capabilities[18,19]. In these self-healing systems, metal-ligand coordination bonds have been successfully and broadly used in self-healing polymer materials with the advantages of rich metal-ligand species[20,21], selectable and adjustable coordination bond strengths (25 to 95% of covalent bonding)[22], as well as functionalities of different coordination systems (stimulation correspondence, shape memory, and luminescence, etc.)[23].

However, the vast majority of metal-ligand coordination bonds either have excessively stable bond strengths or are too weak to be suitable for constructing self-healing polymer materials[24]. To address these challenges, researchers have developed innovative strategies targeting the synthesis of new ligands and polymers, aiming to achieve metal-coordinated polymer materials with self-healing properties[25,26]. However, incorporating ligands into polymer systems often involves elaborate chemical synthesis, leading to greatly elevated costs and difficulties in industrial application compared to hydrogen and ionic systems. Additionally, the metal-coordinated polymer materials frequently lack ultra-high electrical conductivity ($> 1.0\times10^5$ $S\cdot m^{-1}$) and thermal conductivity (> 2 W/m·K), which significantly restricts their applications in modern technologies[27,28].

Liquid metals (LMs) have drawn considerable interest in the fields of flexible electronics and wearable devices owing to their fluidity at room temperature and exceptional thermal/electrical conductivity[29-33]. However, gallium (Ga)-based liquid metals exhibit weak coordination ability with common ligands and, like aluminum (Al) metals, have thus been rarely studied in metal-coordination systems[34,35]. In recent years, dissolving other metals in liquid metals to create functionalized multi-component LMs (mLMs) has gained significant attention. For instance, dissolving palladium in Ga can result in new catalytic materials with fluidity[36]. Mixing metallic iron with Ga builds a magnetic metal with high mobility[37]. Our team has also successfully dissolved metals such as bismuth and indium in liquid Ga to prepare phase change materials with high thermal conductivity for electronic heat dissipation and packaging[38]. Therefore, coordination-active metals such as silver (Ag) and zinc (Zn) are introduced into liquid metals (LMs) to endow the resulting multi-component liquid metals (mLMs) with coordination capabilities. The fluidic interfaces of mLMs microdroplets enable regeneration of coordination sites through interfacial atomic migration, thereby expanding the dynamic coordination unit from molecular to microscopic dimensions. This mLMs-based dynamic interfacial strategy can derive its reversibility from the self-renewing fluidic interface, rather than being constrained by the strength of coordination bonds.

In contrast, existing reversible coordination systems rely on weak bonding interactions at the molecular dimensions, where their reversible behavior remains confined by the inherent strength of the coordination bonds.

In this work, through the mLMs interfacial coordination bonds, we creatively leverage the inherent fluidity of mLMs to convert classical metal-ligand coordination into reversible interfacial interactions and endow general polymers with self-healing capabilities. This work introduces a wide range of metal-coordinated bonds into self-healing polymer systems. It thereby overcomes a critical limitation of conventional systems, where the bonds are either too strong or too weak to enable complete and autonomous healing. In this work, silver-sulfur coordination is fully investigated as a representative mLMs system and successfully achieved reversible coordination behaviors at the mLMs interfaces, offering the self-healing properties for natural rubber (NR). The coordination composites show excellent self-healing efficiencies of over 90% under room temperature. More importantly, such mLMs strategy can be applied to common metal-ligand coordination bonds and is suitable for general polymers. For example, zinc and copper-imidazole coordination are also introduced into liquid metal systems to achieve the surprisingly self-healing feature for general acrylic polymers with self-healing efficiency over 90%. Molecular dynamics (MD) simulations, Materials Studio (MS) calculations, mechanical evaluations and X-ray photoelectron spectroscopy (XPS) analysis strongly demonstrated the dynamic interfacial characteristics of mLMs surface atoms and their ligand coordination capability. Considering the thermal performance of mLMs, self-healable thermal interface materials (TIMs) are obtained with high thermal conductivity (6.8 W/m·K). The self-healable TIMs successfully address the long-standing challenge of irreversible damage in long-term used high-performance TIMs, which can lower the peak temperature of the central processing unit (CPU) by 20 ^{o}C under extreme conditions for long time (accumulated 16 hours thermal shock from -10 ^{o}C to 100 ^{o}C). This work creatively combines LMs and metal coordination chemistry, which provides a universal and powerful strategy for the next generation of functional self-healable materials.

Results

Gallium is not suitable for use in metal-ligand coordination based self-healing polymers because of its weak metal coordination ability. Interestingly, liquid metal Ga acts as a metal solvent. This property allows the synthesis of coordination-active mLMs through the incorporation of metals such as silver (Ag), copper (Cu), and zinc (Zn). As shown in Fig. 1A, the introduction of mLMs into the polymer system resulted in successful interfacial coordination between the active metal atoms on the surface of the mLMs and the ligands on the polymer chains. Unlike a common metal-ligand coordination system, this interfacial coordination occurs exclusively around the active metal atoms on the surface of the fluidic mLMs. The fluidity of mLMs plays a critical role in the reversible interfacial coordination for self-healing involving mLMs and polymer materials. Fig. 1B illustrates the self-healing process of interfacial coordination. Firstly, interfacial coordination is formed between the active metal atoms on the surface of mLMs and ligands (Fig. $1B_1$). When damaged by external force, defective regions are generated on the surface of mLMs, and the interfacial coordination formed between mLMs and ligands is simultaneously damaged (Fig. $1B_2$). Then, due to the fluidity of mLMs, the newly generated active metal atoms and Ga in the defective region migrate to the surface and heal the defects. The healed mLMs surface re-engages with the ligands on the polymer chains, thereby enabling the self-healing features (Fig. $1B_3$). In contrast, realizing the self-healing capability by common strong metal coordination systems (such as Ag-S) is challenging, as demonstrated in Fig. 1C. Owing to the abundant active sites on Ag powder, strong Ag-S coordination bonds form between the powder and sulfur ligands in natural rubber

(NR), creating a rigid network. The permanent and irreversible nature of the coordination bond at the interface makes it difficult for the composite to exhibit self-healing properties.

Interestingly, the mLMs strategy can make common metal coordination (e.g., the above Ag-Sulfur coordination) into dynamic interfacial coordination and provide self-healing properties for general polymers. As shown in Fig. 1D and Fig. S1, the stretchable mLMs-NR composites containing 30 wt.% $Ag_{0.1}$LMs dispersed in NR are prepared by shear mixing designated as $Ag_{0.1}$LMs-NR-30. Here, mLMs-Polymer-*y* is used to represent the composition of the sample in this work. *m* is the active metal in the LM, *x* is the weight ratio between the m and LM, *y* is the weight percentage of the m and LM in the composites and polymer is the base material. The interfacial coordination of $Ag_{0.1}$LMs endows $Ag_{0.1}$LMs-NR-30 with fantastic self-healing capability. As shown in Fig. $1E_1$, the damaged area of the composite completely heals after 180 min at room temperature, with the healed material maintaining tensile properties comparable to the original state (Fig. $1E_2$).

Based on the dynamic interfacial coordination formed between mLMs and ligands, the autonomous healing capability of mLMs composites is further demonstrated. As shown in Fig. 2A, the damaged $Ag_{0.1}$LMs-NR-30 achieved successful self-healing performance within 180 min at room temperature. Uniaxial tensile experiments further show that the self-healed samples retained tensile capacity under large strains (0, 300 and 450%). This phenomenon can be attributed to the reversible interfacial coordination between polysulfide ligands and $Ag_{0.1}$LMs in the composite. Upon mechanical damage, the fluidity of $Ag_{0.1}$LMs facilitates interfacial diffusion and reformation of coordination bonds, enabling self-healing capability while maintaining mechanical performance. In addition, DSC analysis of $Ag_{0.1}$LMs-NR-30 shows no melting peak (Fig. S2A), confirming the liquid state of $Ag_{0.1}$LMs from 0 - 80 ^{o}C. This fluidity is maintained due to the supercooling effect of micro-sized LM droplets in the composite matrix (Fig. S2B) [39]. In addition, the self-healing properties of the $Ag_{0.1}$LMs-NR-y composites with different filler mass fractions (y = 0, 10, 30 and 50) are systematically investigated. As shown in Fig. S3, when $Ag_{0.1}$LMs is in excess ($y > 50$), it reduces the mechanical strength of the material due to the agglomeration of mLMs in composites. In contrast, at low loading ($y < 30$), the interfacial coordination network is defective due to insufficient coordination density. This results in decreased self-healing efficiency. The incorporation of $Ag_{0.1}$LMs with liquidity interfaces dramatically improves the autonomous healing performance of the $Ag_{0.1}$LMs-NR-30 (Fig. 2B). $Ag_{0.1}$LMs-NR-30 exhibits almost the same mechanical behaviors with the original sample after 180 min of self-healing (Fig. 2B), indicating effective self-healing properties. Furthermore, 3D microscopy images (Fig. 2B, inset) reveal that the microcrack interfaces at the fracture surface are progressively repaired as healing time increases (Fig. S4), directly confirming the self-healing capability of $Ag_{0.1}$LMs-NR-30 composite. Notably, pure NR polymer exhibits an extremely low self-healing efficiency of 2.4% (Fig. S5), whereas NR polymer with 30 wt.% $Ag_{0.1}$LMs ($Ag_{0.1}$LMs-NR-30) significantly enhances self-healing efficiency to 90.5%. Furthermore, as demonstrated in Fig. 2C, when pure Ga is composited with NR, Ga-NR-30 (the weight fraction of Ga in the composite is 30 wt.%) has a self-healing efficiency of only 11.3%, confirming the critical role of coordination interactions at the interface. In contrast, Ag-NR-3 (3.0 wt.% Ag) displays negligible self-healing efficiency (0.8%), which originates solely from polymer chain diffusion (Fig. 2C and S5). This system represents a traditional strong metal-coordination system that lacks interfacial liquidity. Upon increasing the Ag mass fraction to 30%, the resulting Ag-NR-30 exhibits poor moldability. This is attributed to the fact that the excess Ag coordinates with sulfide bonds, which shows too heavy crosslinking to impair the molding process (Fig. S5). The mechanism of the self-healing ability can be further elucidated by microstructural analyses. The SEM images and element mapping in Fig. 2D show that the damaged region is enriched with coordination-active Ag and liquid Ga. Importantly, the fluidic Ga transports Ag to the damaged area, reconstructing an interface capable of coordinating with ligands in the polymer matrix and thereby enabling self-healing (Fig. S6). Fig. 2E demonstrates that the healing efficiency of $Ag_{0.1}$LMs-NR-30 exhibits a time-dependent enhancement, reaching 90.5% after 180 minutes of healing under room temperature. In addition, the $Ag_{0.1}$LMs-NR-30 has excellent self-healing stability with healing efficiency over 86% in five fracture-healing cycle tests (Fig. S7). The self-healing rate of composites is ultimately limited by polymer chain mobility. As shown in Fig. S8, with identical $Ag_{0.1}$LMs content, the low molecular weight NR composite ($Ag_{0.1}$LMs-L-NR-30) reaches 90% healing efficiency in just 120 minutes. The relatively higher molecular weight NR composite ($Ag_{0.1}$LMs-NR-30) is 60 minutes slower to complete self-healing. This marked difference confirms that chain migration and rearrangement kinetics govern macroscopic healing behavior. The hysteresis curves from mechanical cycling can effectively characterize the interfacial healing processes within the materials[40]. As shown in Fig. 2F, the cyclic tensile curve of $Ag_{0.1}$LMs-NR-30 after healing (strain: 200%) almost completely overlaps with that of the original sample, indicating significant recovery of its elastic properties. Notably, during the cycling tests, the hysteresis curve of $Ag_{0.1}$LMs-NR-30 gradually decreases with increasing tensile cycles but fully recovers to its initial state after 30 minutes of rest (Fig. S9). This phenomenon is attributed to the rupture-reconstruction mechanism of the dynamic interfacial coordination between $Ag_{0.1}$LMs and sulfide bonds, which not only recovers the elastic properties but also ensures exceptional stability under repeated loading. In contrast, the hysteresis curve of Ag-NR-3 remains unaffected by increasing cycle numbers (Fig. S10), which is closely related to its highly stable crosslinked network within the polymer. The strong coordination interactions significantly suppress relative sliding between molecular chains, yet limit the ability of the material to self-heal. However, Ga-NR-30 exhibits high residual strain even after 30 minutes of rest following 200% strain stretching, demonstrating irreversible structural damage (Fig. S10). Further insight into the interfacial dynamics comes from rheological analysis. As shown in Fig. S11, the $Ag_{0.1}$LMs-NR-30 composite exhibits simultaneously decreasing storage and loss moduli with temperature, characteristic of a dynamic network enabled by interfacial fluidity. In contrast, the Ag-NR-3 composite shows constant moduli, reflecting a static, irreversible network. These results further confirm the critical role of the dynamic interfacial coordination in self-healing performance.

More importantly, the reversible interfacial coordination strategy establishes a universal approach for coordination-mediated self-healing, enabling the construction of high-performance self-healing materials by common coordination bonds. As shown in Fig. 2G, the introduction of the interfacial coordination system of Zn-imidazole into polymer materials can also obtain excellent self-healing composites. When mechanical damage occurs, interfacial fracture develops within the composite. The $Zn_{0.2}$LMs at the fracture interface spontaneously coordinate with imidazole ligands on polymer chains, driving reconstruction of coordination networks that eliminate cracks and enabling self-healing of composites. To demonstrate the healing mechanism, polymers containing imidazole ligands were synthesized through a facile one-pot free radical polymerization method. The monomers (n-butyl acrylate (nBA), 1-vinylimidazole (Vim) and methyl methacrylate (MMA)) were selected to copolymerize to obtain PBVM copolymer (P(nBA-co-Vim-co-MMA)) **(**the synthetic procedure is shown in Fig. S12)**.** The ^{1}H NMR spectrum and Fourier infrared (FT-IR) results indicate successful copolymerization (Fig. S13 - S14). The obtained PBVM is solvent blending with $Zn_{0.2}$LMs to form the $Zn_{0.2}$LMs-PBVM-12 composite. As shown in Fig. 2H, the cut sample of $Zn_{0.2}$LMs-PBVM-12 (0.2 g) achieves self-healing and supports a 200 g load, demonstrating its high load-bearing capacity and structural stability. Optical microscopy observations reveal that microcracks disappear completely after 18 hours of healing. Furthermore, mechanical tensile tests reveal a 91.9% self-healing efficiency for the $Zn_{0.2}$LMs-PBVM-12 after

18 hours at room temperature (Fig. 2I). In addition, the self-healing capability of $Zn_{0.2}$LMs-PBVM-12 originates from $Zn_{0.2}$LMs-driven coordination interactions. As a result, pure PBVM materials do not show self-healing properties **(**Fig. S15**)**. Similarly, Zn-PBVM-2.4 (without Ga) and Ga-PBVM-12 (without Zn) are also unable to self-heal. These control experiments confirm that both fluidic character and coordination ability are indispensable for achieving self-healing. In addition, similar self-healing behaviors are also observed for the copper-imidazole system. With the same PBVM polymer, $Cu_{0.05}$LMs-PBVM-6 showed the self-healing efficiency near 90% **(**Fig. S16**)**, indicating the broad applicability of the reversible interfacial coordination strategy for common metal-ligand systems.

The fabrication process of mLMs is shown in Fig. $3A_1$, the mLMs are obtained by doping Ag or Zn reactive metal particles in Ga matrix at high temperature (~250 °C). Ag or Zn active metals are uniformly dispersed as atoms or atomic clusters within the mLMs. Notably, the obtained mLMs are also fluidic metals near room temperature, which is verified by dynamic scanning calorimetry (DSC) with melting temperatures at 33.4 ^{o}C and 29.4 ^{o}C, respectively (Fig. S17 - S18). The self-healing process of mLMs is illustrated in Fig. $3A_2$. When mLMs are damaged, their intrinsic mobility enables the atoms to migrate to the damaged surface, thereby forming the renewable surface character for mLMs. The fluidity of mLMs allows coordination-active atoms to migrate between adjacent droplets. EDS analysis in Fig. S19 shows that Ag atoms transferred through the liquid Ga matrix from Ag-rich to Ag-poor droplets until reaching compositional equilibrium. This inter-droplet mobility enables network redistribution of Ag atoms, significantly enhancing the efficiency of the self-healing process. To investigate the dispersion state of Ag in the $Ag_{0.1}$LMs matrix, molecular dynamics (MD) simulations are performed using the LAMMPS software under canonical ensemble system (NVT) conditions at a temperature of 537.15 K, for a duration of 100 ps with a time step of 1 fs, and a mixing potential truncation radius of 10.0 Å, constructing an

$Ag_{0.1}$LMs model system composed of 2304 Ga atoms and 256 Ag atoms (Fig. S20). Fig. 3B demonstrates the RDF of the atoms of the $Ag_{0.1}$LMs bulk region, which shows that the radial distances of the different atom pairs in the system are Ag-Ag (2.7 Å), Ga-Ga (2.8 Å) and Ag-Ga (3.5 Å), respectively. Atomic configuration analysis confirms that Ag atoms are uniformly dispersed as isolated atoms or small clusters within the $Ag_{0.1}$LMs model, with no significant aggregation observed. The distribution of Ag atoms at the interface is consistent with that in the bulk region (Fig. S21A). Additionally, the atomic density distribution along the Z-direction reveals that Ag atoms are uniformly distributed in the $Ag_{0.1}$LMs model, with a slight shift toward the interface (Fig. S21B). SEM and elemental mapping reveal that $Ag_{0.1}$LMs form spherical droplets with smooth surfaces (Fig. 3C). Surface analysis detects both Ga and Ag, confirming the presence of active Ag atoms at the liquid interface. The green areas correspond to regions enriched with Ga, whereas the red areas indicate Ag atoms distributed on the surface of $Ag_{0.1}$LMs particles, confirming the presence of Ag atoms at the liquid interface. Zn atoms are also identified on the surface of $Zn_{0.2}$LMs (Fig. S22). Similarly, as shown in Fig. 3D, the XRD spectra of $Ag_{0.1}$LMs exhibited characteristic peaks corresponding to Ag and Ga, along with distinct Ag_3Ga phase peaks detected at approximately 23.6°, 40° and 47.7°. It is noteworthy that similar phase formation and elemental dispersion behavior were observed in the $Zn_{0.2}$LMs (Fig. S23).

Based on the atomic distribution characteristics of mLMs, the active Ag atoms uniformly distributed at the mLMs interface can form active sites capable of coordination with functional ligands. Interestingly, coupled with the inherent fluidity, the interfacial active region in mLMs also exhibits fluidity and thus shows damage-reconstruction, endowing a renewable interfacial coordination feature for mLMs after surface damage. XPS analyses further confirmed the atomic structure features of the mLMs interface. As shown in Fig. 3E, the characteristic peaks of Ga 2p and Ag 3d are observed simultaneously on the surface of $Ag_{0.1}$LMs. Notably, the characteristic peaks of Ga 2p and Ag 3d are still observed on the newly exposed surface after interfacial damage with consistent peak positions and intensities. This result clearly demonstrates the distinctive liquid-like interfacial self-healing of $Ag_{0.1}$LMs. And mechanism relies on their inherent fluidity, which enables spontaneous reorganization after interfacial damage. More importantly, as shown in Fig. S24**,** the Ag 3d peak of $Ag_{0.1}$LMs shifts to a higher binding energy (0.6 eV) compared to conventional Ag powder. The higher binding energy indicates the polarization of Ag atoms and similar results are observed in previous reports[36]. The Ag atoms on the surface of $Ag_{0.1}$LMs are polarized by the local environment in liquid metal Ga, leading to partial positive electroneutrality of Ag atoms. Similar to previous work[41,42], these polarized metal atoms provided anchor points for coordination at the interface with the polymer, and the entire polymer chain interacts with the $Ag_{0.1}$LMs by coordination adsorption, providing the basis for material self-healing. The surface atomic activity of mLMs plays a crucial role in the renewable interfacial coordination. As shown in Fig. 3F, the Linear Scanning Voltammogram (LSV) polarization curves of Ga, $Ag_{0.1}$LMs, and $Zn_{0.2}$LMs are presented. The results indicate that the overpotentials for $Ag_{0.1}$LMs and $Zn_{0.2}$LMs are significantly lower than those of Ga at current densities of 20 $mA \cdot cm^{-2}$ and 50 $mA \cdot cm^{-2}$. As previous reported[43], the lower overpotentials suggested that the reaction kinetics of the mLMs are faster (Fig. S25), which further highlights the high reactivity of Ag and Zn atoms located on the surface of mLMs. Materials Studio (MS) calculations demonstrate significant differences in the interaction of Ag, Ga and $Ag_{0.1}$LMs with sulfur (Fig. S26). As shown in Fig. 3G, the strong Ag-S binding energy results from coordination bonding. This creates a rigid interfacial structure that prevents self-healing. In contrast, Ga exhibits a lower binding energy with S, only 61% of the binding energy of Ag to S, making it challenging for Ga surfaces to effectively anchor S atoms. For $Ag_{0.1}$LMs, the binding energy is intermediate between pure Ag and Ga, compared to pure Ag-S coordination, the $Ag_{0.1}$LMs weakened the binding between Ag and S by reducing the exposure of Ag atoms, which is favorable for the renewable interfacial coordination. Furthermore, the XPS spectrum of Fig. S27 shows a characteristic peak of Ag-S coordination bonding in the S 2p spectrum of $Ag_{0.1}$LMs-NR-30. In contrast, no similar peak is observed for Ga-NR-30. These results further supported the existence of Ag-S coordination at the interface for $Ag_{0.1}$LMs. In addition, the significantly weaker Ag-S peak in $Ag_{0.1}$LMs-NR-30 compared to Ag-NR-3 further confirms that Ag atoms are diluted in the Ga matrix, resulting in fewer effectively exposed atoms at the interface and demonstrating the dynamic nature of the liquid Ga interface (Fig. S27 C, D). For the Zn-imidazole coordination system, the ability of $Zn_{0.2}$LMs and Ga to coordinate with the imidazole ligand is evaluated by sedimentation experiments. As shown in Fig. 3H, in the PBVM solution with dichloromethane as the solvent (50 mg/mL), $Zn_{0.2}$LMs remained well dispersed in the PBVM solution for 24 h, whereas Ga exhibited significant sedimentation as early as 12 hours. This difference demonstrates the coordination between the imidazole groups in the PBVM solution and $Zn_{0.2}$LMs. Additionally, the XPS characterization **(**Fig. 3I**)** further confirms the mechanism of interfacial coordination. In the N 1s spectrum, the imidazole functional group (C-N=) in $Zn_{0.2}$LMs-PBVM-12 shows a 0.12 eV shift toward lower energy compared to PBVM (Fig. S28). In contrast, the same functional group in the pure Ga system does not exhibit an obvious shift.

The above studies demonstrate the notable benefits of mLMs-polymer composites for self-healing properties. Given the excellent thermal conductivity of mLMs, the self-healable mLMs-polymer composites will be excellent TIMs for modern electronics. The central processing unit (CPU), as the data processing center in a computer, generates significant heat and becomes a key high-temperature component on the motherboard (Fig. S29). To address this challenge, we fabricate $Ag_{0.1}$LMs-NR films (70 wt.% filler) that combine the high thermal conductivity of $Ag_{0.1}$LMs with the flexibility of NR, yielding excellent thermal dissipation. These films are applied as TIMs between the CPU and the heat sink. As shown in Fig. 4A**,** the $Ag_{0.1}$LMs-NR-70 film covers the

CPU surface, and the flexibility of the $Ag_{0.1}$LMs-NR-70 film makes it to conform closely to the CPU surface, effectively eliminating air gaps and thereby improving heat dissipation efficiency. As shown in Fig. 4B, the thermal conductivity of $Ag_{0.1}$LMs-NR-70 films increases significantly with increasing $Ag_{0.1}$LMs filler loading. At 70 wt.% $Ag_{0.1}$LMs filler content, $Ag_{0.1}$LMs-NR-70 exhibits a thermal conductivity of 3.2 W/m·K. When the filler content is increased to 90 wt.%, the thermal conductivity rose to 6.8 W/m·K, a 20-fold enhancement over pure NR. Further, At the same filler mass fraction, the thermal conductivity of $Ag_{0.1}$LMs-NR-70 is increased by 33.3% compared to Ga-NR-70, indicating that the Ag atoms in $Ag_{0.1}$LMs form coordination with the sulfur atoms in the molecular chain of NR, thereby lowering the interfacial thermal resistance and significantly enhancing the thermal conductivity (Fig. S30). The prepared $Ag_{0.1}$LMs-NR-70 films demonstrated high thermal conductivity and outperformed most reported Ga-based thermally conductive composites fabricated via the simple shear-mixing method (Table S1). In addition, due to polymer barrier effect, the $Ag_{0.1}$LMs-NR-70 films exhibits excellent electrical insulation properties and prevented leakage of $Ag_{0.1}$LMs, even at a high filler content of 70 wt.% (Fig. S31). Flexible and highly thermally conductive $Ag_{0.1}$LMs-NR-70 films are utilized as advanced TIMs to be further evaluated by a CPU. Fig. 4C and Fig. S32 present the infrared thermography and temperature-time curves with the CPU running at 100% power loading. The CPU covers with NR film exhibited a significant increase in temperature during operation, reaching an operating temperature of approximately 100 °C in 120 seconds. In contrast, the CPU covered with $Ag_{0.1}$LMs-NR-70 films exhibited a gradual increase in temperature from 40 °C to 64 °C during the first 60 seconds, then stabilized at approximately 68 °C at 120 seconds. The $Ag_{0.1}$LMs-NR-70 demonstrated a significant reduction in CPU operating temperature, achieving a decrease of 32 °C compared to NR films without $Ag_{0.1}$LMs. Additionally, as a control, the CPU covered with Ga-NR film operated at a temperature approximately 4 °C higher than that of the $Ag_{0.1}$LMs-NR-70 films, which was stabilized at about 72 °C. The results demonstrated that $Ag_{0.1}$LMs-NR-70 and Ga-NR-70 films were able to effectively reduce the rate of temperature rise and peak temperature during CPU operation.

Although Ga-NR-70 and $Ag_{0.1}$LMs-NR-70 possess similar thermal conductivity, the self-healing property of $Ag_{0.1}$LMs-NR-70 ensures its long-term thermal management efficiency. As shown in Fig. 4D, the damages created by the blade-scratching on $Ag_{0.1}$LMs-NR-70 surface gradually disappeared over time and fully healed after 6 hours under near room temperature. In contrast, the scratches on the Ga-NR-70 surface under the same conditions did not show obvious changes after 6 h (Fig. S33). The self-healing properties of $Ag_{0.1}$LMs-NR-70 films enable them to maintain efficient thermal management. As shown in Fig. 4E, interfacial damage in the $Ag_{0.1}$LMs-NR-70 films reduced their heat transfer efficiency, which in turn raised the maximum CPU temperature by 6 °C compared to the initial state. However, after 6 h of self-healing, the thermal performance of the healed $Ag_{0.1}$LMs-NR was effectively restored, with the maximum CPU temperature dropping to about 68 ℃, which was similar as the intact $Ag_{0.1}$LMs-NR-70.

The self-healable TIMs in this work will successfully address the long-standing industrial challenge[44-46] of the irreversible damage in long-term used TIMs. Fig. 4F evaluates the long-term stability of $Ag_{0.1}$LMs-NR-70 and Ga-NR-70 under extreme conditions. $Ag_{0.1}$LMs-NR-70 and Ga-NR-70 films were treated with harsh thermal shocks from -10 °C to 100 °C for different cycles (0 - 500 times, accumulative 16 hours, see supplementary information for detailed thermal shock experiment). The treated TIMs were covered on the working CPU (100% power loading) and the real-time temperature of the CPU was monitored. During the long-term 500 cycles of harsh thermal shocks, CPUs with $Ag_{0.1}$LMs-NR-70 TIMs exhibited nearly constant working temperature at initial 68 °C to final 73 °C (Fig. 4F). In sharp contrast, after 16 hours intensive thermal shock treatment, the temperature of the CPU covered with Ga-NR-70 TIMs increased from 72 ^{o}C to 93 ^{o}C in about 250 cycles of the extreme thermal shocks. The surface changes of the films during the extreme thermal shocks were further observed by SEM images (Fig. 4F, insets). Initially, the surface of Ga-NR-70 was smooth and defect-free, exhibiting no visible defects or cracks. In contrast, Ga-NR-70 developed surface irregularities, voids, and cracks after the 16 hours thermal shock treatment. These defects hindered heat transfer and compromised the material's performance. However, the $Ag_{0.1}$LMs-NR-70 TIM exhibits no obvious change on its surface due to the self-healing capability to heal the surface micro-cracks to maintain its thermal conductivity at 2.9 W/m·K (Fig. S34). Finally, Fig. 4G presents the real-time maximum CPU temperature for the thermally shocked Ga-NR-70 TIM. The temperature rise to 93°C after 120 seconds of operation. In contrast, the CPU covers with the $Ag_{0.1}$MLs-NR-70 treated with the same extreme conditions shown much better heat dissipation performance by stabilizing the temperature at about 73 °C after 120 seconds. The above results indicate that the dynamic interfacial LM coordination strategy could be a highly promising route to address the long-standing industrial challenge for the long-term stability of high-performance TIMs.

Discussion

In summary, this work combines LMs and metal coordination chemistry to convert most of the current irreversible metal-ligand bonds into reversible interfacial interactions, which can offer the desirable self-healing feature for general polymers. The reversible coordination behavior at the mLMs interfaces successfully offers the self-healing properties with healing efficiency over 90% for general polymers via silver-sulfur and zinc/cooper -imidazole coordination systems. Molecular simulations (e.g., MD and MS), mechanical characterization, and XPS analysis strongly supported the dynamic interfacial characteristics of mLMs surface atoms and their ligand interaction capability. Multi-functional TIMs with combined high thermal conductivity and self-healing performance were obtained and successfully addressed the long-standing challenge of irreversible damage in TIMs under harsh environments, showing long-term stability and exceptional damage recovery capability. This work will extremely broaden the studies of self-healing materials, coordination chemistry, liquid metal science, soft electronics, thermal management materials, and many other fields, which should be highly interesting for lots of scientists in material science and engineering.

Methods

Materials: Gallium (Ga, 99.999%, melting point: 29.8 ^{o}C) was purchased from Changge Shuochen Metal Co., Ltd. Silver powder (Φ: 25 μm, 99.9995%, melting point: 961.8 ^{o}C) was purchased from Nangong Xindun Alloy Welding Spraying Co., Ltd. Zinc powder (Φ: 20 μm, 99.99%, melting point: 419.5 ^{o}C), copper powder (Φ: 22 μm, 99.99%, melting point: 1083.4 ^{o}C), Sulfur (S8, AR, 99.5%), other rubber additives (zinc oxide, ZnO, AR, 99%, stearic acid, Sta, GC, 95%; N-cyclohexyl benzothiazole-2-sulfenamide, CZ, HPLC, 98%) and methyl methacrylate (MMA, GC, 99.0%) were purchased from Shanghai Aladdin Bio-Chem Technology Co., Ltd. Natural rubber (NR, complex viscosity η^* = 454 kPa·s, 100 ^{o}C) was purchased from Hainan Rubber Industrial Co., Ltd, China, Low molecular weight rubber (L-NR, complex viscosity η^* = 155 kPa·s, 100 ^{o}C) was purchased from Hong Manli Rubber Products Co., Ltd. 1-Vinylimidazole (VIM, 99%), n-butyl acrylate (BA, CP, 98%), dichloromethane (DCM, AR, 99.5%), and 2-hydroxy-2-methylpropiophenone (HMPP, 99%) were purchased from Shanghai McLean Biochemical Technology Co. Ltd.

Preparation of metal-polymer composite: (1) $Ag_{0.1}$LMs: The metals Ga (18 g), Ag (2 g) (mass ratio of Ga: Ag = 9: 1) were put in a 10 mL round-bottom flask. The mixtures were then heated in an electric heater above 250 ^{o}C (melting point of Ga: 29.8 ^{o}C, Ag: 961.8 ^{o}C) under a nitrogen atmosphere until all metals got melted. After a slight cooling (about 100 ^{o}C), the melt was mechanically stirred at 500 rpm to ensure homogeneity. Finally, the $Ag_{0.1}$LMs were obtained by moving the flask out of the electric heater and cooling the mixture at room temperature for 30 min. (2) The $Zn_{0.2}$LMs (Ga: Zn mass ratio 8:2, 16 g Ga and 4 g Zn) and $Cu_{0.05}$LMs (Ga: Cu mass ratio 19:1, 19 g Ga and 1 g Cu) were prepared in the same way as $Ag_{0.1}$LMs. (3) $Ag_{0.1}$LMs-NR-*y*: The preparation of $Ag_{0.1}$LMs-NR-*y* composites with 15% mass fraction was taken as an example. NR (10 g), rubber additives (ZnO (0.5 g), SA (0.2 g), CZ (0.12 g)), Sulfur (0.12 g) and $Ag_{0.1}$LMs (4.7 g) were sequentially added to an open mill (STD-2KL) and shear-mixed at 60 ^{o}C at 30 rpm for 15 minutes to ensure uniform dispersion of the filler. The 0.5-mm-thick $Ag_{0.1}$LMs-NR-30 composite was fabricated by hot-pressing the mixture at 150 ^{o}C under 20-ton pressure for 16 minutes with a dumbbell-shaped mold and a melt-compounder (AP2113, AUPLEX). Other samples with different filler contents were prepared using the method described above. (4) PBVM: in a typical free-radical co-polymerization procedure, VIM (1.37 g, 14.6 mmol), BA (5.23 g, 40.9 mmol), MMA (0.29 g, 2.9 mmol) and Photoinitiator HMPP (0.048 g, 0.292 mmol) (mole ratio of VIM: BA: MMA=5: 14: 1) were placed into a bottle equipped with a magnetic stirrer, and irradiated under UV light (365 nm) for 10 min, PBVM had been obtained. (5) $Zn_{0.2}$LMs-PBVM-*y*: PBVM (1 g) was dissolved in dichloromethane (20 mL) and stirred at 400 rpm for 12 h at 45 ^{o}C to ensure complete dissolution, forming a viscous PBVM solution. Following this, $Zn_{0.2}$LMs (0.12 g) was added to the solution and manually ground with a pestle at room temperature until $Zn_{0.2}$LMs was uniformly dispersed in the solution. The mixture was then transferred to a vial and stirred at 400 rpm at 45 ^{o}C for 24 h. Finally, the mixture was poured into a polytetrafluoroethylene mold, left to evaporate at room temperature for 4 h, and subsequently dried in an oven at 80 ^{o}C for 12 h to obtain the $Zn_{0.2}$LMs-PBVM-12 composite. Comparative samples were prepared using the same procedure.

Instruments: mLMs were mixed by LED Digital Overhead Stirrer (DLAB 8033100200 OS20-S) and heated by electric heater mantle (PTHW250ML). The mLMs and natural rubber (NR) were mixed by an open mill (STD-2KL) and a melt-compounder (AP2113, AUPLEX) to obtain mLMs-NR composites. Oven (DZF-6020) was used to control the temperature and maintain an isothermal condition. An oven (DZF-6020) was used to control the temperature and remove solvents from the mLMs-PBVM composites. The surface structure of the mLMs-polymer composite was observed by a digital microscope (Leica DVM6). The mechanical and self-healing performance of mLMs-polymer composites was performed on a universal testing machine (MTS E42). The microstructure and healing process of mLMs and mLMs-NR composites were characterized by a Field Emission Scanning Electron Microscope (FEI Inspect F50). The Energy-dispersive X-ray spectroscopy (EDS) of mLMs-NR composites was used to characterize the element distributions. The chemical compositions of samples were characterized by the X-ray photoemission spectrometer (XPS, ESCALAB 250Xi) with Al Kα radiation (λ = 1486.6 eV). X-ray diffraction (XRD) was measured with Ultima IV. The mLMs were loaded onto quartz glass for measurement. Scanning range: 5° - 110°, scanning speed: 5 °/min, optical grating: 5mm. Gel Permeation Chromatography (GPC) The PL-GPC 220 (Polymer Laboratories) was operated to measure samples at 40 ^{o}C with DMF as mobile phase. The functional group components of PBVM were characterized by using Fourier transform infrared spectroscopy (FT-IR) Characterization. ^{1}H nuclear magnetic resonance (^{1}H NMR) spectroscopy was performed on the Avance III HD 600 MHz 300 MHz spectrometer. Differential scanning calorimetry (DSC) characterization was carried out using the DSC25 thermal analyzer (TA) instruments to characterize thermal transitions. The samples (5~10 mg) were loaded into DSC pans, then quenched to -50 °C and subsequently heated to 60 °C at a rate of 5 °C/min. The thermal conductivity of NR, Ga-NR and $Ag_{0.1}$LMs-NR films was measured on a thermal conductivity tester (XIATECH TC3000E). It should be noted that the measured value of thermal conductivity was the apparent thermal conductivity. The general tests were performed at room temperature. The rheology data of the samples was collected by a rheometer Discover HR20, TA Instruments. All the samples were fabricated into a small round sheet ($\Phi = 20 \pm 0.5$ mm, $H = 2 \pm 1$ mm). The temperature sweep was in oscillation mode from 30 to 200 ^{o}C with 10 ^{o}C /min at 10 rad/s, 3.0% strain.

Data Availability

The data generated in this study are provided in the Source Data file. All data are available in the main text or the supplementary information. Source data are provided with this paper. All data are available from the corresponding author upon request.

References

1. Wang, S., Urban, M.W. Self-healing polymers. *Nat. Rev. Mater.* **5**, 562–583 (2020).
2. Y. Zhou, L. Li, Z. Han, Q. Li, J. He, Q. Wang, Self-Healing Polymers for Electronics and Energy Devices. *Chem. Rev.* **123**, 558–612 (2023).
3. A. C. Cornellà, F. Furia, G. Van Assche, J. Brancart, Controlling the Relaxation Dynamics of Polymer Networks by Combining Associative and Dissociative Dynamic Covalent Bonds. *Adv. Mater.* **36**, e2407663 (2024).
4. J. Jung, S. Lee, H. Kim, W. Lee, J. Chong, I. You, J. Kang, Self-healing electronic skin with high fracture strength and toughness. *Nat. Commun.* **15**, 9763 (2024).
5. C. Choi, J. L. Self, Y. Okayama, A. E. Levi, M. Gerst, J. C. Speros, C. J. Hawker, J. Read de Alaniz, C. M. Bates, Light-Mediated Synthesis and Reprocessing of Dynamic Bottlebrush Elastomers under Ambient Conditions. *J. Am. Chem. Soc.* **143**, 9866–9871 (2021).

6. Y. Yanagisawa, Y. Nan, K. Okuro, T. Aida, Mechanically robust, readily repairable polymers via tailored noncovalent cross-linking. *Science* **359**, 72–76 (2018).
7. Y. Chen, A. M. Kushner, G. A. Williams, Z. Guan, Multiphase design of autonomic self-healing thermoplastic elastomers. *Nat. Chem.* **4**, 467–472 (2012).
8. J.-Y. Sun, X. Zhao, W. R. K. Illeperuma, O. Chaudhuri, K. H. Oh, D. J. Mooney, J. J. Vlassak, Z. Suo, Highly stretchable and tough hydrogels. *Nature* **489**, 133–136 (2012).
9. M. Wang, X. Xiao, S. Siddika, M. Shamsi, E. Frey, W. Qian, W. Bai, B. T. O'Connor, M. D. Dickey, Glassy gels toughened by solvent. *Nature* **631**, 313–318 (2024).
10. M. Nakahata, Y. Takashima, H. Yamaguchi, A. Harada, Redox-responsive self-healing materials formed from host–guest polymers. *Nat. Commun.* **2**, 511 (2011).
11. N. Nitta, M. Takatsuka, S. Kihara, T. Hirao, T. Haino, Self-Healing Supramolecular Materials Constructed by Copolymerization via Molecular Recognition of Cavitand-Based Coordination Capsules. *Angew. Chem. Int. Ed.* **59**, 16690–16697 (2020).
12. C.-H. Li, C. Wang, C. Keplinger, J.-L. Zuo, L. Jin, Y. Sun, P. Zheng, Y. Cao, F. Lissel, C. Linder, X.-Z. You, Z. Bao, A highly stretchable autonomous self-healing elastomer. *Nat. Chem.* **8**, 618–624 (2016).
13. D. Mozhdehi, S. Ayala, O. R. Cromwell, Z. Guan, Self-Healing Multiphase Polymers via Dynamic Metal–Ligand Interactions. *J. Am. Chem. Soc.* **136**, 16128–16131 (2014).
14. M. Burnworth, L. Tang, J. R. Kumpfer, A. J. Duncan, F. L. Beyer, G. L. Fiore, S. J. Rowan, C. Weder, Optically healable supramolecular polymers. *Nature* **472**, 334–337 (2011).
15. K. Sato, T. Nakajima, T. Hisamatsu, T. Nonoyama, T. Kurokawa, J. P. Gong, Phase-Separation-Induced Anomalous Stiffening, Toughening, and Self-Healing of Polyacrylamide Gels. *Adv. Mater.* **27**, 6990–6998 (2015).
16. S. Bonardd, M. Nandi, J. I. Hernández García, B. Maiti, A. Abramov, D. Díaz Díaz, Self-Healing Polymeric Soft Actuators. *Chem. Rev.* **123**, 736–810 (2023).
17. S. Lee, J. Kum, S. Kim, H. Jung, S. An, S. J. Choi, J. H. Choi, J. Kim, K. J. Yu, W. Lee, H. Kim, H.-S. Han, M. Shin, H. Kim, D. Son, A shape-morphing cortex-adhesive sensor for closed-loop transcranial ultrasound neurostimulation. *Nat. Electron.* **7**, 800–814 (2024).

18. C. C. M. Sproncken, P. Liu, J. Monney, W. S. Fall, C. Pierucci, P. B. V. Scholten, B. Van Bueren, M. Penedo, G. E. Fantner, H. H. Wensink, U. Steiner, C. Weder, N. Bruns, M. Mayer, A. Ianiro, Large-area, self-healing block copolymer membranes for energy conversion. *Nature* **630**, 866–871 (2024).
19. A. Pena-Francesch, H. Jung, M. C. Demirel, M. Sitti, Biosynthetic self-healing materials for soft machines. *Nat. Mater.* **19**, 1230–1235 (2020).
20. B. Li, P.-F. Cao, T. Saito, A. P. Sokolov, Intrinsically Self-Healing Polymers: From Mechanistic Insight to Current Challenges. *Chem. Rev.* **123**, 701–735 (2023).
21. E. Khare, N. Holten-Andersen, M. J. Buehler, Transition-metal coordinate bonds for bioinspired macromolecules with tunable mechanical properties. *Nat. Rev. Mater.* **6**, 421–436 (2021).
22. J.-F. Gohy, Metallo-supramolecular block copolymer micelles. *Coord. Chem. Rev.* **253**, 2214–2225 (2009).
23. C. Li, J. Zuo, Self-Healing Polymers Based on Coordination Bonds. *Adv. Mater.* **32**,e1903762 (2020).
24. C. Liang, V. Dudko, O. Khoruzhenko, X. Hong, Z.-P. Lv, I. Tunn, M. Umer, J. V. I. Timonen, M. B. Linder, J. Breu, O. Ikkala, H. Zhang, Stiff and self-healing hydrogels by polymer entanglements in co-planar nanoconfinement. *Nat. Mater.* **24**, 599–606 (2025).
25. Y. Shi, B. Wu, S. Sun, P. Wu, Aqueous spinning of robust, self-healable, and crack-resistant hydrogel microfibers enabled by hydrogen bond nanoconfinement. *Nat. Commun.* **14**, 1370 (2023).
26. L. Zhang, J. B. Bailey, R. H. Subramanian, A. Groisman, F. A. Tezcan, Hyperexpandable, self-healing macromolecular crystals with integrated polymer networks. *Nature* **557**, 86–91 (2018).
27. J. Kang, D. Son, G. N. Wang, Y. Liu, J. Lopez, Y. Kim, J. Y. Oh, T. Katsumata, J. Mun, Y. Lee, L. Jin, J. B. -H. Tok, Z. Bao, Tough and Water-Insensitive Self-Healing Elastomer for Robust Electronic Skin. *Adv. Mater.* **30**, e1706846 (2018).
28. J. Chen, Y. Zhou, X. Huang, C. Yu, D. Han, A. Wang, Y. Zhu, K. Shi, Q. Kang, P. Li, P. Jiang, X. Qian, H. Bao, S. Li, G. Wu, X. Zhu, Q. Wang, Ladderphane copolymers for high-temperature capacitive energy storage. *Nature* **615**, 62–66 (2023).

29. S. Liu, D. S. Shah, R. Kramer-Bottiglio, Highly stretchable multilayer electronic circuits using biphasic gallium-indium. *Nat. Mater.* **20**, 851–858 (2021).

30. Y. Zhao, Y. Ohm, J. Liao, Y. Luo, H.-Y. Cheng, P. Won, P. Roberts, M. R. Carneiro, M. F. Islam, J. H. Ahn, L. M. Walker, C. Majidi, A self-healing electrically conductive organogel composite. *Nat. Electron.* **6**, 206–215 (2023).

31. X. Ni, H. Luan, J.-T. Kim, S. I. Rogge, Y. Bai, J. W. Kwak, S. Liu, D. S. Yang, S. Li, S. Li, Z. Li, Y. Zhang, C. Wu, X. Ni, Y. Huang, H. Wang, J. A. Rogers, Soft shape-programmable surfaces by fast electromagnetic actuation of liquid metal networks. *Nat. Commun.* **13**, 5576 (2022).

32. H. Liu, Y. Xin, H. K. Bisoyi, Y. Peng, J. Zhang, Q. Li, Stimuli-Driven Insulator–Conductor Transition in a Flexible Polymer Composite Enabled by Biphasic Liquid Metal. *Adv. Mater.* **33**, e2104634 (2021).

33. S. A. Idrus-Saidi, J. Tang, S. Lambie, J. Han, M. Mayyas, M. B. Ghasemian, F.-M. Allioux, S. Cai, P. Koshy, P. Mostaghimi, K. G. Steenbergen, A. S. Barnard, T. Daeneke, N. Gaston, K. Kalantar-Zadeh, Liquid metal synthesis solvents for metallic crystals. *Science* **378**, 1118–1124 (2022).

34. L. Duan, T. Zhou, Y. Zhang, J. Zhao, J. Zhang, Q. Li, J. Liu, Q. Liu, Colourful liquid metals. *Nat. Rev. Mater.* **7**, 929–931 (2022).

35. T. Daeneke, K. Khoshmanesh, N. Mahmood, I. A. de Castro, D. Esrafilzadeh, S. J. Barrow, M. D. Dickey, K. Kalantar-zadeh, Liquid metals: fundamentals and applications in chemistry. *Chem. Soc. Rev.* **47**, 4073–4111 (2018).

36. J. Tang, A. J. Christofferson, J. Sun, Q. Zhai, P. V. Kumar, J. A. Yuwono, M. Tajik, N. Meftahi, J. Tang, L. Dai, G. Mao, S. P. Russo, R. B. Kaner, Md. A. Rahim, K. Kalantar-Zadeh, Dynamic configurations of metallic atoms in the liquid state for selective propylene synthesis. *Nat. Nanotechnol.* **19**, 306–310 (2024).

37. W. Xiang, Y. Lu, H. Wang, X. Sun, S. Chen, Z. He, J. Liu, Liquid-metal-based magnetic fluids. *Nat. Rev. Mater.* **9**, 433–449 (2024).

38. H. Wang, Y. Peng, H. Peng, J. Zhang, Fluidic phase–change materials with continuous latent heat from theoretically tunable ternary metals for efficient thermal management. *Proc. Natl. Acad. Sci. U.S.A.* **119**, e2200223119 (2022).

39. J. Yan, M. H. Malakooti, Z. Lu, Z. Wang, N. Kazem, C. Pan, M. R. Bockstaller, C. Majidi, K. Matyjaszewski, Solution processable liquid metal nanodroplets by surface-initiated atom transfer radical polymerization. *Nat. Nanotechnol.* **14**, 684–690 (2019).

40. J. Xu, Y. Li, T. Liu, D. Wang, F. Sun, P. Hu, L. Wang, J. Chen, X. Wang, B. Yao, J. Fu, Room-Temperature Self-Healing Soft Composite Network with Unprecedented Crack Propagation Resistance Enabled by a Supramolecular Assembled Lamellar Structure. *Adv. Mater.* **35**, e2300937 (2023).

41. Y. Lei, F. Mehmood, S. Lee, J. Greeley, B. Lee, S. Seifert, R. E. Winans, J. W. Elam, R. J. Meyer, P. C. Redfern, D. Teschner, R. Schlögl, M. J. Pellin, L. A. Curtiss, S. Vajda, Increased Silver Activity for Direct Propylene Epoxidation via Subnanometer Size Effects. *Science* **328**, 224–228 (2010).

42. P. Liu, R. Qin, G. Fu, N. Zheng, Surface Coordination Chemistry of Metal Nanomaterials. *J. Am. Chem. Soc.* **139**, 2122–2131 (2017).

43. C. Yang, G. Rousse, K. Louise Svane, P. E. Pearce, A. M. Abakumov, M. Deschamps, G. Cibin, A. V. Chadwick, D. A. Dalla Corte, H. Anton Hansen, T. Vegge, J.-M. Tarascon, A. Grimaud, Cation insertion to break the activity/stability relationship for highly active oxygen evolution reaction catalyst. *Nat. Commun.* **11**, 1378 (2020).

44. X. C. Tong, Advanced Materials for Thermal Management of Electronic Packaging (Springer, 2011).

45. N. Burger, A. Laachachi, M. Ferriol, M. Lutz, V. Toniazzo, D. Ruch, Review of thermal conductivity in composites: Mechanisms, parameters and theory. *Prog. Polym. Sci.* **61**, 1–28 (2016).

46. G.-H. Kim, D. Lee, A. Shanker, L. Shao, M. S. Kwon, D. Gidley, J. Kim, K. P. Pipe, High thermal conductivity in amorphous polymer blends by engineered interchain interactions. *Nat. Mater.* **14**, 295–300 (2015).

Acknowledgments

The work was supported by National Key Research and Development Program of China under Grant (grant number 2023YFB4404200, to J.Y.Z.). Basic Research Program of Jiangsu (Grant No. BK20241359, to Y.P.; BK20250075, to J.Y.Z.).

Author Contributions

J.Y.Z. proposed the idea and conceived the project. J.Y.Z., Z.W.L., and Y.Z. designed the experiments and performed the experiments. J.Y.Z., Z.W.L., Y.Z., S.L.L., J.Y.L. and P.Y. analyzed the results of the experiments for data. J.Y.Z., Z.W.L. and J.Y.L. wrote the manuscript. All authors commented on the manuscript.

Competing Interests

The patents for this strategy (NO. 2025109379401) have been submitted to the China Patent Office. The patent application (CN2025109379401) has been filed by Southeast University with inventors J.Y.Z., Z.W.L., and P.Y. The applicants for the related patents of this manuscript are author J.Y.Z., Z.W.L., and P.Y. declare that there are no other conflicts of interest related to this research. The remaining authors, Y.Z., S.L.L., and J.Y.L., who did not participate in the patent application, also declare that there are no competing interests.

Figure Captions

Fig. 1: Self-healing mechanisms by dynamic interfacial coordination of mLMs. (A) mLMs form interfacial coordination bonds with ligands on the polymer chain. mLMs atomic-scale micrograph (left) and mLMs are uniformly dispersed in the polymer and interact with their ligands (center), microscopic enlargement of the interfacial coordination of active metal atoms at the surface of mLMs (right)**. (B)** Self-healing process for dynamic interfacial coordination between mLMs and polymers. **(B_1)** Interfacial coordination between ligands and surface-active metal atoms on mLMs; (**B_2**) When damaged, defects are generated on the surface of mLMs; (**B_3**) The surface

is restructured with the fluidic mLMs, thus re-forming the interfacial coordination bonds to achieve healing; Re-coordination (abbreviated as Re-Coord.). **(C)** Non-self-healable materials formed by pure Ag metal particles and polymer chains with ligands. Atomic Ag (left) forming strong normal coordination bonds with the polymer material (right). **(D)** Photographs of highly deformable mLMs/NR (Natural Rubber) composites (mLMs are Ag-Ga alloys with a mass fraction of 30 wt.% in the composite, where the Ag to Ga mass ratio is 1:9, designated as $Ag_{0.1}$MLs). **(E)** Photographs of the healing process of mLMs-NR composites, which were damaged with holes **(E_1)** and stretchable again after 180 min healing **(E_2)**, Scale bar, 25 mm.

Fig. 2: Self-healing properties of mLMs composites. **(A)** Evaluation of damage-healing properties of $Ag_{0.1}$LMs-NR-30 composites. **(A_1-A_2)** Dumbbell-type specimens are completely cut into two parts and underwent healing for 180 min under room temperature. The inset shows the dynamic coordination between $Ag_{0.1}$LMs and sulfur ligands in the self-healed $Ag_{0.1}$LMs-NR-30. **(A_3)** Photographs of healed $Ag_{0.1}$LMs-NR-30 under different tensile strains (strains of 0%, 300%, and 450%). **(B)** Tensile stress-strain curves of $Ag_{0.1}$LMs-NR-30: original sample and after autonomous healing for 30, 90, and 180 min at room temperature. The inset displays 3D optical profilometry images of cracks in the damaged area (left) and after 180 min self-healing (right). color bar: 0 - 40 μm. **(C)** Representative tensile stress-strain plots of non-self-healable Ag-NR-3 and Ga-NR-30 composites. The dashed lines indicate the stress-strain curves of the samples healed for 180 min after cutting. The inset shows the zoom-in part in the early 110% strain of the tensile curves. **(D)** The EDS (Energy Dispersive X-ray Spectroscopy) elemental distribution and scanning electron microscope (SEM) images of the damaged and healed $Ag_{0.1}$LMs-NR-30 sample. Red, green, and yellow dots correspond to S, Ag, and Ga elements, respectively. **(E)** Healing time dependence (30, 90, 180, 720 min) of self-healing efficiency for $Ag_{0.1}$LMs-NR-30 composites. Self-healing efficiency is defined as the area ratio between healed and original stress-strain curves.

Data are the mean ± s.d.; *n*= 3. **(F)** Cyclic stress-strain curves of $Ag_{0.1}$LMs-NR-30 at 200% strain (stretching rate: 20 mm/min). Dashed lines indicate the healed sample re-tested after complete damage and 180 min self-healing. **(G)** Schematic diagram of the self-healing mechanism for $Zn_{0.2}$LMs-PBVM-12 composite (PBVM is a copolymer of n-butyl acrylate (nBA), 1-vinylimidazole (Vim), and methyl methacrylate (MMA)). **(H)** Load-bearing capacity of self-healed $Zn_{0.2}$LMs-PBVM-12 composites. **(H_1)** After 18 h of self-healing, the $Zn_{0.2}$LMs-PBVM-12 composites (0.2 g) can withstand a load of 200 g. Optical microscopy images of $Zn_{0.2}$LMs-PBVM-12 composites: as-cut damaged state **(H_2)** and restored structure after 18 h self-healing **(H_3)**. **(I)** The tensile stress-strain curves of the original $Zn_{0.2}$LMs-PBVM-12 composites and their damaged samples under varying self-healing durations (4, 8, and 18 h).

Fig. 3: Structure of mLMs and dynamic interfacial coordination mechanism. (A) Schematic diagram of the fluidity and self-healing performance of mLMs. **(A_1)** Active metal particles (Ag, Zn, etc.) dissolve in liquid Ga at ~250 °C to form mLMs. **(A_2)** Self-healable mLMs through active metal migration towards the damaged interface. **(B)** Radial distribution function (RDF) of Ag and Ga atoms in $Ag_{0.1}$LMs according to molecular dynamics (MD) simulations. The inset shows a representative screenshot of the atomic configuration of $Ag_{0.1}$LMs. **(C)** The EDS elemental distribution and SEM images of the $Ag_{0.1}$LMs. Red, green dots correspond to Ag and Ga elements, respectively. Scale bar: 10 μm. **(D)** The X-ray diffraction (XRD) spectra of $Ag_{0.1}$LMs. **(E)** XPS full spectra of $Ag_{0.1}$LMs before and after damage. The magnified inset on the right clearly displays the Ag 3d peak. **(F)** Anodic Linear Scanning Voltammogram (LSV) profiles of $Ag_{0.1}$LMs, Ga, and $Zn_{0.2}$LMs in 1 M KOH (scan rate: 10 mV/s). At both 20 and 50 $mA \cdot cm^{-2}$ current densities, $Ag_{0.1}$LMs and $Zn_{0.2}$LMs exhibit significantly lower overpotentials than Ga. **(G)** The Ag-S, $Ag_{0.1}$LMs-S, and Ga-S binding energies are simulated using the universal force field (UFF) in Materials Studio. The systems are kinetically optimized for 50 ps at 298 K under stochastic

conditions. A step size of 1 fs and a truncation radius of 12.5 Å are used. The Ag-S binding energy (32.6 kcal/mol) is normalized to 1 as a reference, the relative binding energies of Ga-S and $Ag_{0.1}$LMs-S exhibit values of 0.61 and 0.81, respectively. In the structural diagrams, yellow, blue, and brown spheres represent S, Ag and Ga atoms, respectively. **(H)** The stability of $Zn_{0.2}$LMs and Ga in PBVM solutions (dichloromethane as solvent) is evaluated using sedimentation experiments. $Zn_{0.2}$LMs remained well dispersed in PBVM solution for 24 hours, while Ga exhibited significant sedimentation within 12 hours. **(I)** XPS N 1s spectral analysis of $Zn_{0.2}$LMs-PBVM-12 and Ga-PBVM-12. The coordination of $Zn_{0.2}$LMs to C-N= caused a 0.12 eV energy shift in the C=N binding energy, the uncoordinated -C-NH group showed no obvious shift.

Fig. 4: Self-healable thermal interface materials (TIMs) from $Ag_{0.1}$LMs-NR films. (A) Photograph of the motherboard of a computer with a Central Processing Unit (CPU, Intel Core i3-2120) covered with $Ag_{0.1}$LMs-NR-70 film. Schematic diagram illustrates the working principle of $Ag_{0.1}$LMs-NR-70. The flexible $Ag_{0.1}$LMs-NR film can be laminated between the heat sink and the CPU. **(B)** Thermal conductivity (λ) of $Ag_{0.1}$MLs-NR films with different mass fractions of metals (0%, 30%, 50%, 70%, 90%). Data are the mean ± s.d., $n = 3$. **(C)** Infrared thermography images of CPUs covered with NR, Ga-NR-70, and $Ag_{0.1}$LMs-NR-70 films at different running time (0 s, 10 s, 60 s, and 120 s) during operation at 100% power loading. Top image was the optical photographs of the different films with the same dimensions (30 mm × 30 mm × 0.5 mm). **(D)** Optical microscopic images for surface-damaged $Ag_{0.1}$LMs-NR-70 film before and after different healing times (2 h, 6 h). **(E)** Temperature-time curves of a 100% power loaded CPU covered with damaged and self-healed $Ag_{0.1}$LMs-NR70 film in Fig. 4D. Insets display optical graphs for the samples on the working CPU. **(F)** Durability evaluation of $Ag_{0.1}$LMs-NR-70 and Ga-NR-70 TIMs under extreme conditions. TIMs are processed under different cycles (0-500) of harsh thermal shocks from -10 ^{o}C- 100 ^{o}C (60 s - 60 s). The treated TIMs are covered on CPUs operating at full power

to record the final stabilized temperature versus the number of cycles. The inset shows the SEM images of the film of $Ag_{0.1}$LMs-NR-70 and Ga-NR-70 after 0 and 500 times of thermal shocks. **(G)** After 500 cycles of extreme thermal shock treatment of the films, the temperature-time curves of a CPU covered with as-treated $Ag_{0.1}$LMs-NR-70 and Ga-NR-70 films were recorded. Difference of 20 ^{o}C is observed for these two TIMs.

Editorial Summary

Self-healing polymer materials based on metal–ligand coordination bonds have been extensively utilized for their advantages of rich metal–ligand species and functionalities but the strength of the metal bonds is not easily tunable. Here, the authors introduce coordination metals into liquid metals leveraging the inherent fluidity of multi-component liquid metals to convert common metal-ligand coordination into reversible interfacial coordination.

Peer review information: *Nature Communications* thanks Bing Guo and the other, anonymous, reviewer for their contribution to the peer review of this work. A peer review file is available.

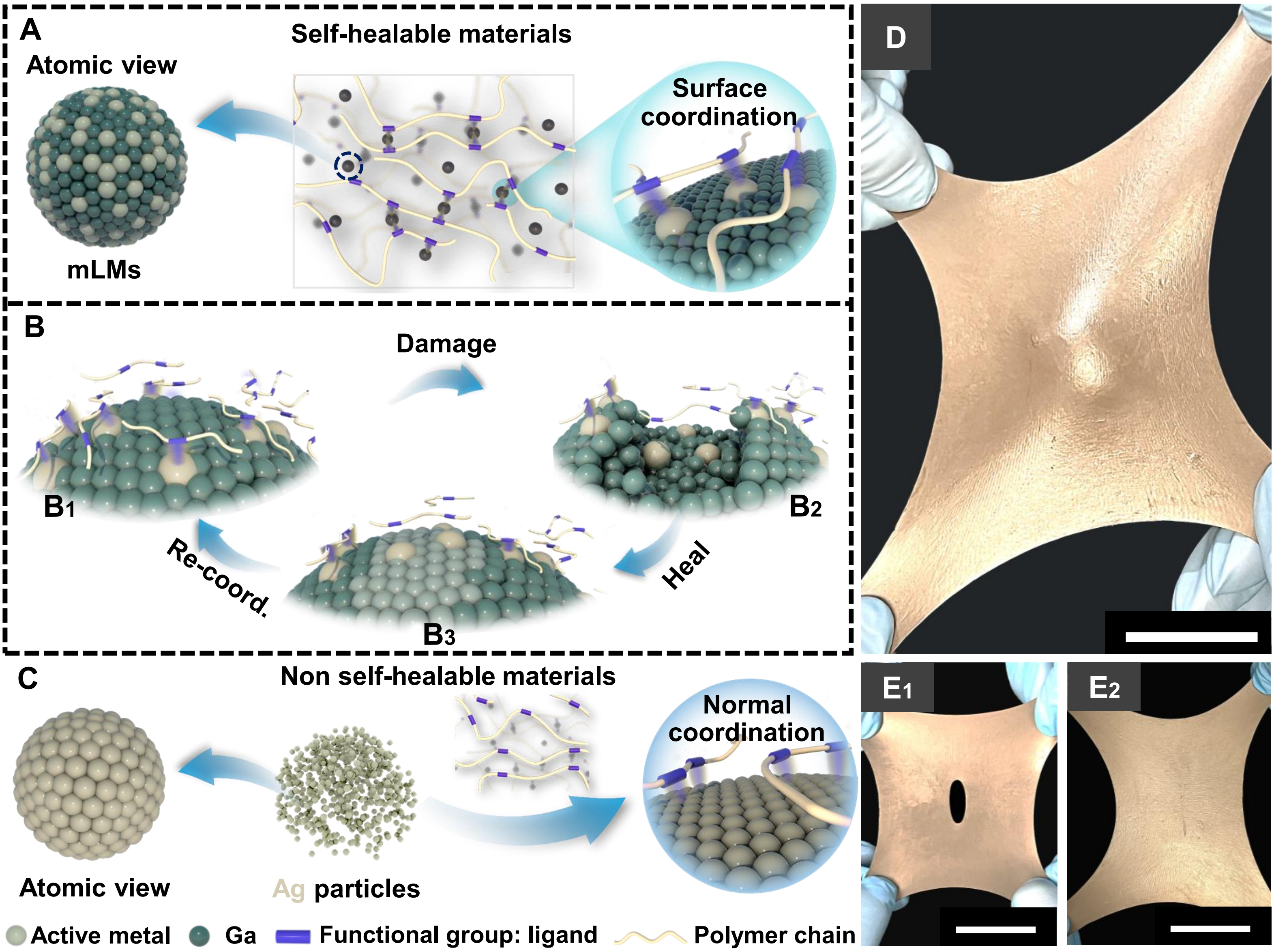
A
Self-healable materials
Atomic view
mLMs
Surface coordination
B
Damage
B1
B2
Heal
Re-coord.
B3
C
Non self-healable materials
Atomic view
Ag particles
Normal coordination
Active metal
Ga
Functional group: ligand
Polymer chain
D
E1
E2

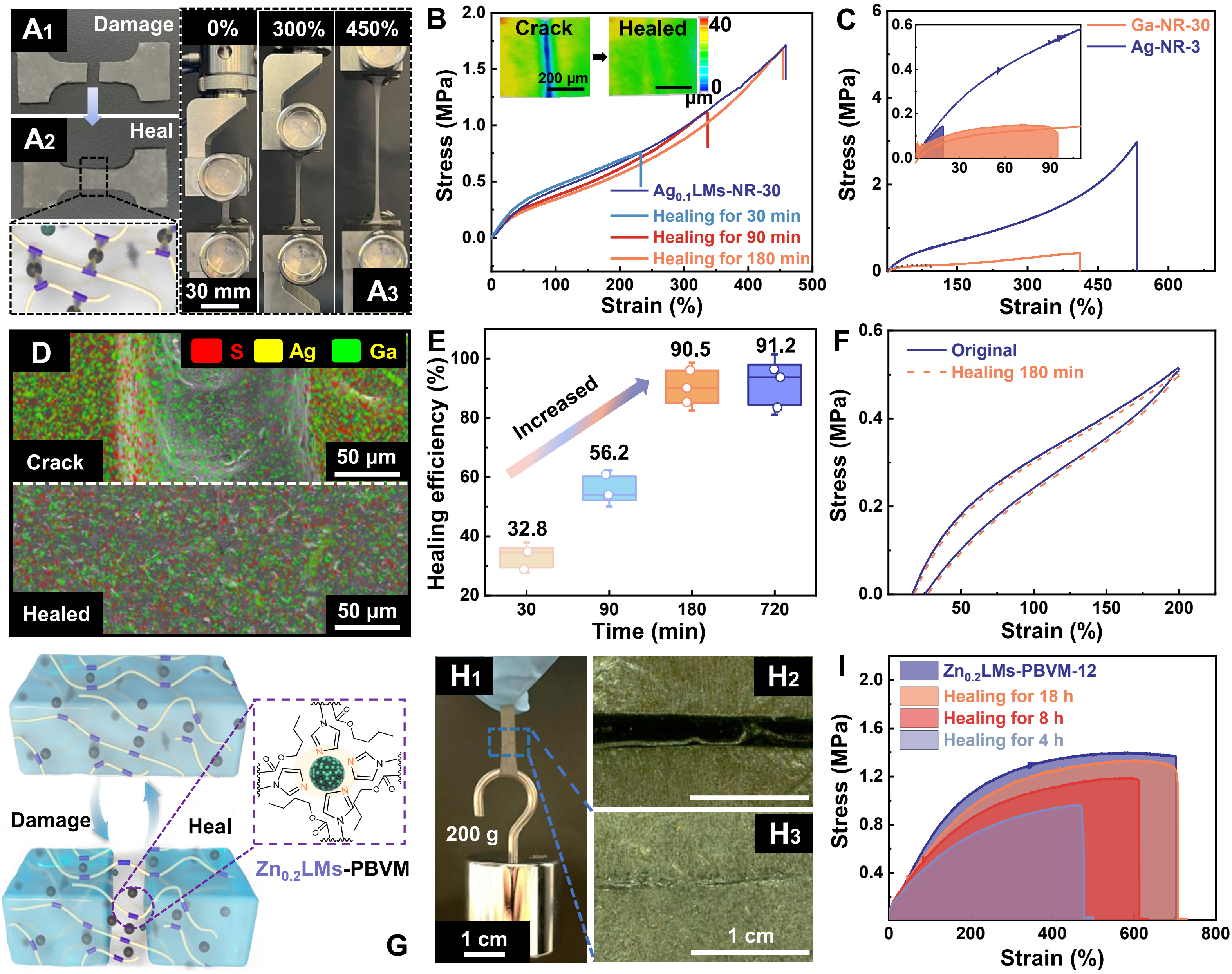
A1
Damage
A2
Heal
0%
300%
450%
30 mm
A3
B
Stress (MPa)
Strain (%)
Crack
Healed
200 µm
40
0
µm
Ag0.1LMs-NR-30
Healing for 30 min
Healing for 90 min
Healing for 180 min
C
Ga-NR-30
Ag-NR-3
Stress (MPa)
Strain (%)
D
S
Ag
Ga
Crack
Healed
50 µm
E
Healing efficiency (%)
Time (min)
Increased
32.8
56.2
90.5
91.2
F
Original
Healing 180 min
Stress (MPa)
Strain (%)
Damage
Heal
Zn0.2LMs-PBVM
G
H1
H2
H3
200 g
1 cm
I
Zn0.2LMs-PBVM-12
Healing for 18 h
Healing for 8 h
Healing for 4 h
Stress (MPa)
Strain (%)

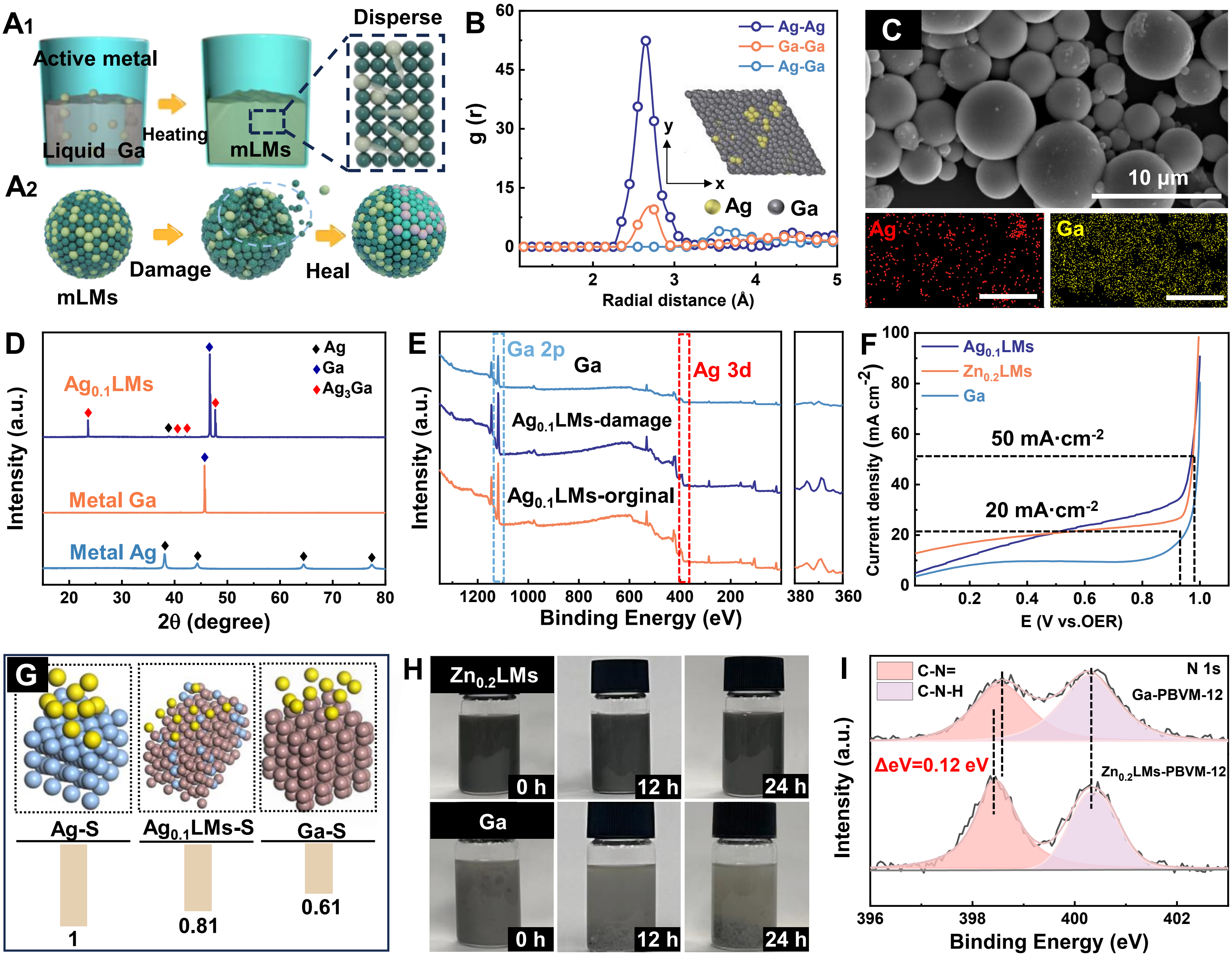
A1
Active metal
Liquid Ga
Heating
mLMs
Disperse
A2
mLMs
Damage
Heal
B
g (r)
Radial distance (Å)
Ag-Ag
Ga-Ga
Ag-Ga
y
x
Ag
Ga
C
10 μm
Ag
Ga
D
Intensity (a.u.)
2θ (degree)
Ag
Ga
Ag_3Ga
$Ag_{0.1}LMs$
Metal Ga
Metal Ag
E
Intensity (a.u.)
Binding Energy (eV)
Ga 2p
Ag 3d
Ga
$Ag_{0.1}LMs$-damage
$Ag_{0.1}LMs$-orginal
F
Current density (mA cm^{-2})
E (V vs.OER)
$Ag_{0.1}LMs$
$Zn_{0.2}LMs$
Ga
50 mA·cm^{-2}
20 mA·cm^{-2}
G
Ag-S
$Ag_{0.1}LMs$-S
Ga-S
1
0.81
0.61
H
$Zn_{0.2}LMs$
Ga
0 h
12 h
24 h
I
Intensity (a.u.)
Binding Energy (eV)
C-N=
C-N-H
N 1s
Ga-PBVM-12
ΔeV=0.12 eV
$Zn_{0.2}LMs$-PBVM-12

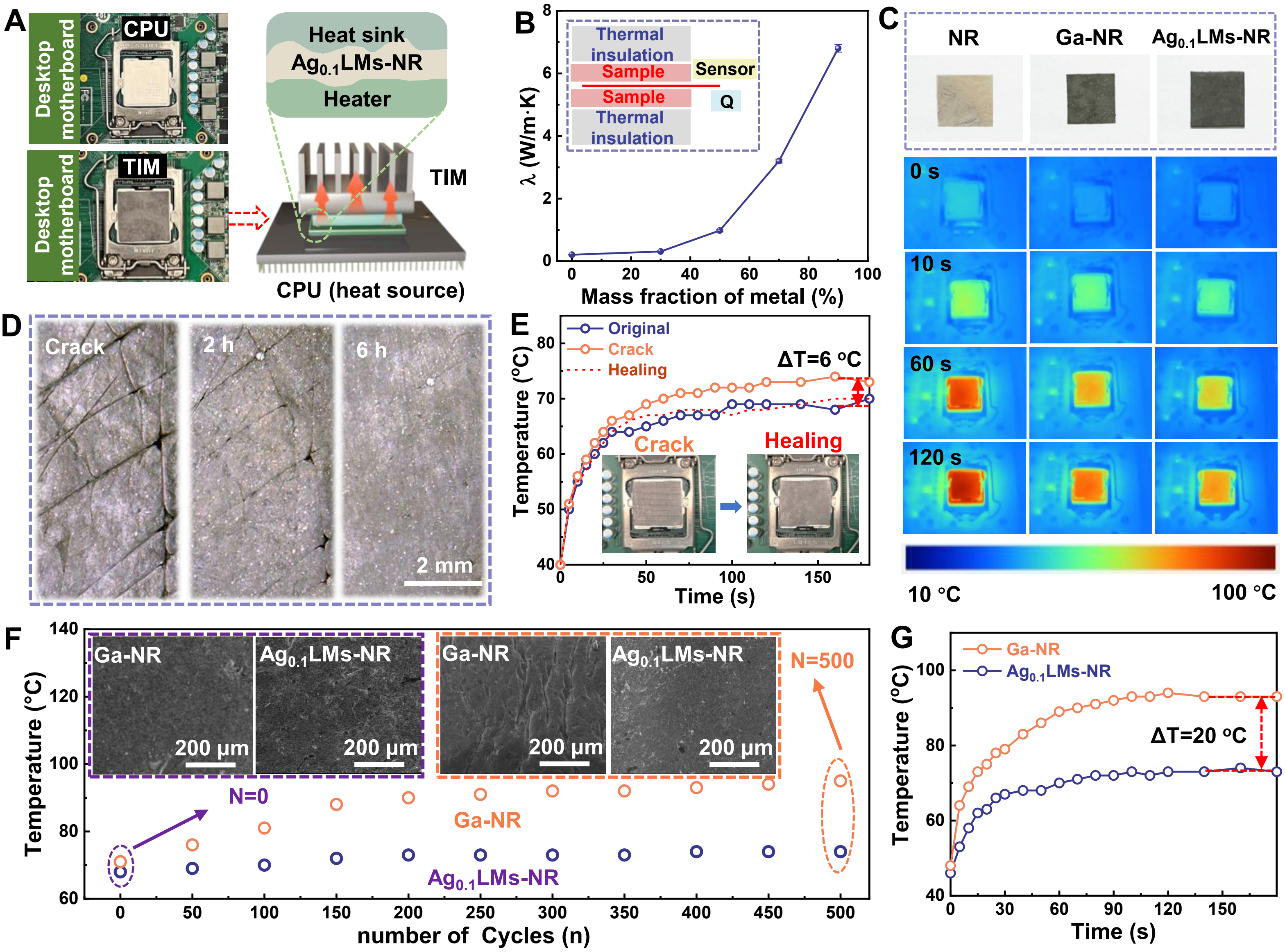
A
Desktop motherboard
CPU
Desktop motherboard
TIM
Heat sink
Ag$_{0.1}$LMs-NR
Heater
TIM
CPU (heat source)
B
λ (W/m·K)
Mass fraction of metal (%)
Thermal insulation
Sample
Sensor
Sample
Q
Thermal insulation
C
NR
Ga-NR
Ag$_{0.1}$LMs-NR
0 s
10 s
60 s
120 s
10 °C
100 °C
D
Crack
2 h
6 h
2 mm
E
Original
Crack
Healing
ΔT=6 °C
Temperature (°C)
Time (s)
Crack
Healing
F
Temperature (°C)
number of Cycles (n)
Ga-NR
Ag$_{0.1}$LMs-NR
Ga-NR
Ag$_{0.1}$LMs-NR
200 μm
N=0
N=500
Ga-NR
Ag$_{0.1}$LMs-NR
G
Ga-NR
Ag$_{0.1}$LMs-NR
ΔT=20 °C
Temperature (°C)
Time (s)